Asociación Argentina
de Mecánica Computacional

Mecánica Computacional Vol XXVII, págs. 3135-3150 (artículo completo)
Alberto Cardona, Mario Storti, Carlos Zuppa. (Eds.)
San Luis, Argentina, 10-13 Noviembre 2008

COMPUTATIONAL STUDY OF LAMINAR SHOCK/BOUNDARY-LAYER INTERACTION AT HYPERSONIC SPEEDS

Gustavo Bono[a], Armando M. Awruch[b] and Tales L. Popiolek[c]

[a]*Federal University of Rio Grande do Sul, Mechanical Engineering Postgraduate Program, Av. Sarmento Leite 425, 90050-170 Porto Alegre, RS, Brazil, bonogustavo@gmail.com, http://www.mecanica.ufrgs.br/promec*

[b]*Federal University of Rio Grande do Sul, Applied and Computacional Mechanical Center, Av. Osvaldo Aranha 99, 90035-190 Porto Alegre, RS, Brazil, amawruch@ufrgs.br, http://www.ppgec.ufrgs.br/cemacom*

[c]*Federal Universitary Foundation of Rio Grande, Mathematical Departament, Av. Itália km 8, Campus Carreiros, 96201-900 Rio Grande, RS, Brazil, dmttales@furg.br, http://www.furg.br*

Keywords: Hypersonic flow, laminar boundary layer, shock wave, finite element method.

Abstract. The principal objective of this paper is to study hypersonic viscous flows dominated by shock-wave / laminar boundary-layer interaction over a compression corner. The shock-wave / boundary-layer interaction is studied using numerical solution of the Navier-Stokes equations for unsteady flows using a Mach number equal to 10.30. The flows are simulated using the Finite Element Method with two explicit Taylor-Galerkin schemes with linear tetrahedral and tri-linear hexahedral elements. Results include surface pressure, skin friction and velocity/pressure/density profiles in several stations.

1 INTRODUCTION

The problem of shock wave / boundary layer interactions (SWBLI) in supersonic and hypersonic flows has been studied for decades (Grasso and Marini, 1996; Dollinger, 2001) due to its direct application in various configurations such as aircraft/spacecraft (control surfaces and wing-fuselage junction), missiles and projectiles, among others. In these configurations the SWBLI has a strong influence in the following items: the levels of heating, the size of the recirculation regions, the loss of efficiency of control surfaces and the oscillation of transient pressure loads.

The geometry formed by the flat plate and the ramp is a typical example in the study of the SWBLI. Although the geometry is simple, the physical phenomena in this problem are very complex; they are the boundary layer separation induced by the shock wave / boundary layer interaction and the strong gradients generated in the recompression region. The main parameters affectting the SWBLI (Bertin, 1994) are: the Mach number, the Reynolds number, the surface temperature, the boundary layer (laminar or turbulent), the deflection angle of the ramp and the chemical state of the gas.

The shock wave / laminar boundary layer interaction (SWLBLI) and the pressure distribution are schematically represented in Figure 1. It is observed that a relatively weak shock is formed at the leading edge of the plate, the shock induced by the ramp interacts with the flat plate boundary layer and, due to the upstream propagation of pressure disturbances across the subsonic portion of the boundary layer, flow separation may occur depending upon the value of the viscous interaction parameter, the Mach number and the wedge angle. The presence of the separation bubble causes the separation and reattachment shocks, whose interaction generates a transmitted shock, a shear layer and, depending upon de Mach number, either a shock wave or an expansion fan that interacts with the boundary layer on the ramp. The pressure, skin friction and heat transfer rapidly increase downstream of the reattachment due to the recompression of the flow, and have a peak immediately after the reattachment in the proximity of the location where the boundary layer thickness is minimum.

An extensive review of the main aspects of laminar supersonic shock-wave boundary-layers interaction phenomena can be found in (Delery, 1988). Early experimental and numerical studies made by Chantz et al. (1998) were on an axisymmetric body shape to avoid three-dimensional effects. In this study was carried out numerous comparisons between different numerical codes (using Navier-Stokes and Direct Monte Carlo Simulation solvers). These studies showed that the separation region is highly sensitive with the mesh and some discrepancies were found between the experimental and numerical pressure in the region of interaction. Similar comparison between the computational results with measurements over a double cone configurations also revealed significant numerical problems can be encountered when predicting the strong gradients generated in regions of shock/shock interaction and boundary layer separations where the differencing schemes can be prone to oscillations and the mesh generation and refinement schemes must be handled with care.

Due to great interest in hypersonic problems, the NATO Research Technology Organization - Advanced Vehicle Technology - Panel Working Group 10 (RTO-TR-AVT-007-V3), proposed some examples for validation of Computational Fluid Dynamics capability for specific flow phenomena relevant to hypersonic flight, which allows a detailed analysis of the influence of different schemes and meshes. The geometry is similar to that shown in Figure 1 and slightly modified with respect to that employed by Chantz et al. (1998). The experiments were conducted for Mach numbers ranging between 10.16 and 12.49 over a range of Reynolds numbers low enough to ensure the flows remained laminar over the model. The

local temperature does not exceed high values where chemical and non-thermal equilibrium effects are initiated. Flow conditions, experimental setup of the 48-inch shock tunnel, and detailed measurements are report in Holden et al. (2006).

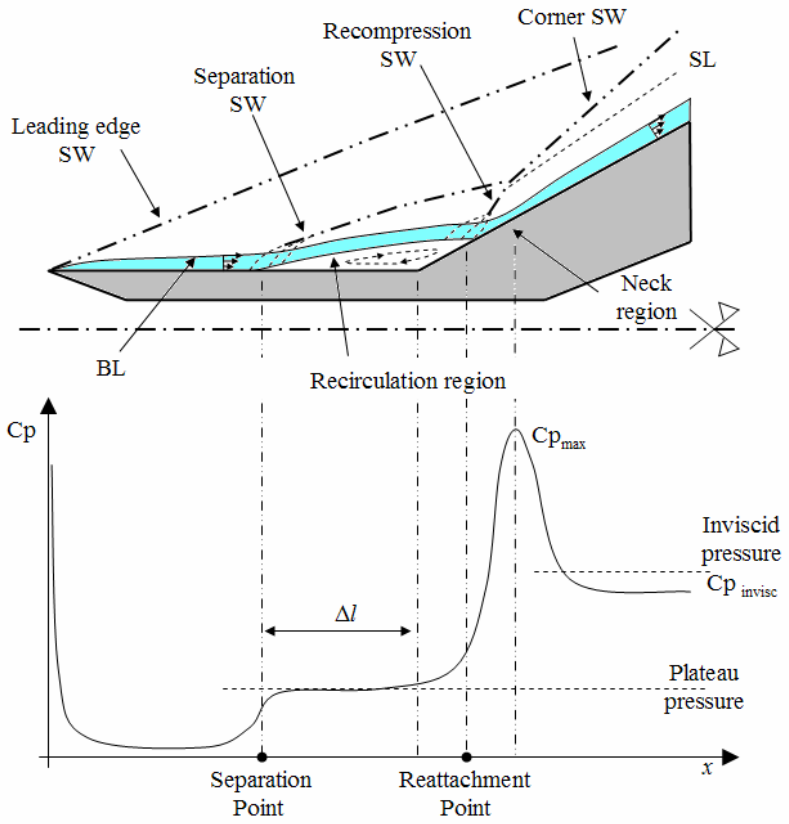

Figure 1: Schematic representation of the shock wave/laminar boundary layer interaction. BL = Boundary Layer, SW = Shock Wave, SL = Shear Layer

In the present work, Navier-Stokes simulations are applied for cold hypersonic gas flow past a compression corner. An in-house developed Navier-Stokes code with structured and unstructured meshes is employed for these computations. The aim of the present work is to study the performance of two explicit Taylor-Galerkin schemes and two types of elements at hypersonic flow. One case is studied and results are compared with experimental and computational results available in the literature.

2 THE GOVERNING EQUATIONS

The most general description of the fluid flow is provided by the time dependent compressible Navier-Stokes equations which express the conservations laws for mass, momentum and energy for viscous fluids.

Let $\Omega \subset R^{n_{sd}}$ and (0,T) be the spatial and temporal domains, respectively, where n_{sd} = 3 is the number of space dimensions, and let Γ denote the boundary of Ω. The spatial and temporal coordinates are denoted by **x** and t. We consider the conservative form of the Navier-Stokes equations governing unsteady compressible flows with no source terms, written here in their dimensionless form

$$\frac{\partial \mathbf{U}}{\partial t}+\frac{\partial \mathbf{F}_i}{\partial x_i}+\frac{\partial \mathbf{G}_i}{\partial x_i}=0 \tag{1}$$

where $\mathbf{U}$ is the unknown vector of the conservation variables, $\mathbf{F}_i$ and $\mathbf{G}_i$ are, respectively, the advective and diffusive flux vectors given by

$$\mathbf{U}=\begin{Bmatrix}\rho\\ \rho v_i\\ \rho e\end{Bmatrix},\qquad \mathbf{F}_i=\begin{Bmatrix}\rho v_j\\ \rho v_i v_j+p\,\delta_{ij}\\ v_j\left(\rho e+p\right)\end{Bmatrix},\qquad \mathbf{G}_i=\begin{Bmatrix}0\\ -\tau_{ij}\\ -\tau_{ji}v_i-q_j\end{Bmatrix} \tag{2}$$

with *i, j = 1,2,3*. Here v_i is the velocity component in the direction of the coordinate x_i, ρ is the specific mass, p is the thermodynamic pressure, τ_{ij} are the components of the viscous stress tensor, q_j is the heat flux vector, e is the total specific energy and δ_{ij} is the Kronecker delta function. For a compressible fluid flow, the following non-dimensional scales are used

$$\begin{aligned} x_i&=\frac{\tilde{x}_i}{\tilde{L}} \qquad v_i=\frac{\tilde{v}_i}{\tilde{a}_\infty} \qquad \rho=\frac{\tilde{\rho}}{\tilde{\rho}_\infty} \qquad e_i=\frac{\tilde{e}_i}{\tilde{a}_\infty^2}\\ p&=\frac{\tilde{p}}{\tilde{\rho}_\infty\,\tilde{a}_\infty^2} \qquad i=\frac{\tilde{c}_v\,\tilde{T}}{\tilde{a}_\infty^2} \qquad t=\frac{\tilde{t}}{\tilde{L}/\tilde{a}_\infty}\end{aligned} \tag{3}$$

where a superscript $\sim$, indicates a dimensional quantity, subscript ∞ represents a reference free stream value, a is a speed of sound and L is a reference length.

For a calorically perfect gas, the equation of state and internal energy i are given by the following equations

$$p=\left(\gamma-1\right)\rho\, i,\qquad i=c_v\,T=e-\frac{1}{2}v_i\,v_i \tag{4}$$

where p is the pressure, T is the temperature and $\gamma=c_p/c_v$ with c_p and c_v being the specific heat coefficients at constant pressure and constant volume, respectively. The viscous stress tensor τ_{ij} and the heat flux vector q_j are defined as

$$\tau_{ij}=\lambda\, v_{k,k}\,\delta_{ij}+\mu\left(v_{i,j}+v_{j,i}\right),\qquad q_j=-k_{ij}\,T_{,k} \tag{5}$$

where *k = 1,2,3*. Here k_{ij} represents the components of the conductivity tensor, λ and μ are the volumetric and dynamic viscosity coefficients, respectively. The dynamic viscosity and coefficient of thermal conductivity depend a temperature and therefore are modeled using Sutherland's law (White, 1974)

$$\mu=\left(\frac{T}{T_{ref}}\right)^{3/2}\frac{T_{ref}+S_\mu}{T+S_\mu},\qquad k=\left(\frac{T}{T_{ref}}\right)^{3/2}\frac{T_{ref}+S_k}{T+S_k} \tag{6}$$

where T_{ref} is the temperature reference and S_μ = 110 K and S_k = 194 K for atmospheric air.

Initial and boundary conditions must be added to equation (1) in order to define uniquely the problem.

3 A TAYLOR-GARLERKIN FORMULATION

The numerical scheme is obtained expanding in Taylor series the governing equation and

applying after the space discretization process, using the Finite Element Method (FEM) in the context of the classical Bubnov-Galerkin scheme. This approach can be interpreted as the finite element version of the Lax-Wendroff scheme used in finite differences. Two schemes for explicit time integration (one-step and two-step methods) are investigated for solving the compressible viscous flow problems.

This time integration provides second-order accuracy for time derivative. The formulation exclusively employs tetrahedral and hexahedral finite elements which provide second-order spatial accuracy. Linear unstructured finite elements were chosen because they can be easily generated for complex geometries and exactly integrated without numerical quadrature. To obtain important savings in CPU time and computer memory, an analytical evaluation of the eight node hexahedral element matrices was performed.

3.1 Time discretization: One-step scheme

The one-step scheme is similar to that presented by Donea (1984). Expanding the conservation variables $\mathbf{U}$ at $t = t^{n+1}$ in Taylor series including the first and second derivatives, it is obtained

$$\Delta\mathbf{U}^{n+1} = \Delta t\left(\frac{\partial\mathbf{U}}{\partial t}\right)^{n+s_1} + \frac{\Delta t^2}{2!}\left(\frac{\partial^2\mathbf{U}}{\partial t^2}\right)^{n+s_2} + O\left(\Delta t^3\right) \tag{7}$$

with $\Delta\mathbf{U}^{n+1} = \mathbf{U}^{n+1} - \mathbf{U}^n$, being s_1 and s_2 the implicitness parameters defined such that

$$\begin{aligned} \frac{\partial\mathbf{U}^{n+s_1}}{\partial t} &= \frac{\partial\mathbf{U}^n}{\partial t} + s_1\frac{\partial\Delta\mathbf{U}^{n+1}}{\partial t} \qquad 0 \le s_1 \le 1 \\ \frac{\partial^2\mathbf{U}^{n+s_2}}{\partial t^2} &= \frac{\partial^2\mathbf{U}^n}{\partial t^2} + s_2\frac{\partial^2\Delta\mathbf{U}^{n+1}}{\partial t^2} \qquad 0 \le s_2 \le 1 \end{aligned} \tag{8}$$

Substituting equation (8) into equation (7), and adopting $s_1 = s_2 = 1/2$, the following expression is obtained

$$\Delta\mathbf{U}^{n+1} = \Delta t\left(\frac{\partial\mathbf{U}^n}{\partial t} + \frac{1}{2}\frac{\partial\Delta\mathbf{U}^{n+1}}{\partial t}\right) + \frac{\Delta t^2}{2}\left(\frac{\partial^2\mathbf{U}^n}{\partial t^2} + \frac{1}{2}\frac{\partial^2\Delta\mathbf{U}^{n+1}}{\partial t^2}\right) \tag{9}$$

Substituting equation (1) and its second derivative into equation (9), and neglecting high-order terms, we obtain

$$\begin{aligned} \Delta\mathbf{U}_{I+1}^{n+1} = \Delta t\left[-\frac{\partial\mathbf{F}_i^{\,n}}{\partial x_i} - \frac{\partial\mathbf{G}_i^{\,n}}{\partial x_i} + \frac{\Delta t}{2}\frac{\partial}{\partial x_k}\left(\mathbf{A}_k^{\,n}\frac{\partial\mathbf{F}_i^{\,n}}{\partial x_i}\right)\right] + \\ + \frac{\Delta t}{2}\left[-\frac{\partial\Delta\mathbf{F}_{iI}^{\,n+1}}{\partial x_i} - \frac{\partial\Delta\mathbf{G}_{iI}^{\,n+1}}{\partial x_i} + \frac{\Delta t}{2}\frac{\partial}{\partial x_k}\left(\mathbf{A}_k^{\,n}\frac{\partial\Delta\mathbf{F}_{iI}^{\,n+1}}{\partial x_i}\right)\right] \end{aligned} \tag{10}$$

where I is an iteration counter, $\Delta\mathbf{F}_i^{n+1} = \mathbf{F}_i^{n+1} - \mathbf{F}_i^n$, $\Delta\mathbf{G}_i^{n+1} = \mathbf{G}_i^{n+1} - \mathbf{G}_i^n$ and $\mathbf{A}_i$ is the convection Jacobian defined as $\mathbf{A}_i = \partial\mathbf{F}_i/\partial\mathbf{U}$ (Hughes and Tezduyar, 1984). In expression (10), the variables at time level $n+1$ are involved in the left and right sides of the equation; therefore it is necessary to use an iterative scheme.

3.2 Time discretization: Two-step scheme

The two-step scheme is similar to that presented by Kawahara and Hirano (1983). In the first step, corresponding to the time interval $[t^n, t^{n+1/2}]$, the unknown vector $\mathbf{U}$ at $t = t^{n+1/2}$ is expanded in Taylor series, it is obtained

$$\Delta\mathbf{U}^{n+1/2} = \left(\frac{\Delta t}{2}\right)\frac{\partial \mathbf{U}^n}{\partial t} + \frac{\left(\Delta t/2\right)^2}{2!}\frac{\partial^2 \mathbf{U}^n}{\partial t^2} + O\left(\Delta t^3\right) \tag{11}$$

with $\Delta\mathbf{U}^{n+1/2} = \mathbf{U}^{n+1/2} - \mathbf{U}^n$. Substituting equation (1) and its second derivative into equation (11), and neglecting high-order terms, gives

$$\Delta\mathbf{U}^{n+1/2} = \frac{\Delta t}{2}\left[-\frac{\partial \mathbf{F}_i^{\,n}}{\partial x_i} - \frac{\partial \mathbf{G}_i^{\,n}}{\partial x_i} + \frac{\Delta t}{4}\frac{\partial}{\partial x_i}\left(\mathbf{A}_i^{\,n}\frac{\partial \mathbf{F}_j^{\,n}}{\partial x_j}\right)\right] \tag{12}$$

In the second step, $\mathbf{U}$ at time t^{n+1} is determined by expanding equation (1) in Taylor series, obtaining the following expression

$$\Delta\mathbf{U}^{n+1} = \Delta t\left(\frac{\partial \mathbf{U}}{\partial t}\right)^n + \frac{\Delta t^2}{2!}\left(\frac{\partial^2 \mathbf{U}}{\partial t^2}\right)^n + O\left(\Delta t^3\right) \tag{13}$$

with $\Delta\mathbf{U}^{n+1} = \mathbf{U}^{n+1} - \mathbf{U}^n$. Substituting equation (1) and its second derivative into equation (13), and neglecting high-order terms, the following expression is obtained

$$\Delta\mathbf{U}^{n+1} = \Delta t\left[-\frac{\partial \mathbf{F}_i}{\partial x_i} - \frac{\partial \mathbf{G}_i}{\partial x_i} + \frac{\Delta t}{2}\frac{\partial}{\partial x_i}\left(\mathbf{A}_i\frac{\partial \mathbf{F}_j}{\partial x_j}\right)\right]^{n+\frac{1}{2}} \tag{14}$$

where the convection Jacobian $\mathbf{A}_i$ is defined as $\mathbf{A}_i = \partial\mathbf{F}_i/\partial\mathbf{U}$ (Hughes and Tezduyar, 1984).

3.3 Spatial discretization

Applying the classical Bubnov-Galerkin weighted residual method in the context of the FEM to equation (10), for the one-step scheme, and equations (12) and (14), for the two-step scheme, spatial discretization are obtained for both cases. Details of the explicit matrix form of equations (10), (12) and (14) can be found in Bono (2008). The computational domain was divided into a finite number of tri-linear hexahedral elements (structured mesh) or linear tetrahedral elements (unstructured mesh). The consistent mass matrix is substituted by the lumped mass matrix and then these equations are solved with an explicit scheme.

The proposed schemes are conditionally stable, and the local stability condition for element *E* is given by

$$\Delta t_E = CS\frac{L_E}{a + \left(v_i\, v_i\right)^{1/2}} \tag{15}$$

where L_E is a characteristic dimension of the element, a is the sound speed and CS is a safety coefficient (in this work the coefficient adopted were CS = 0.1).

In order to stabilize the solution numerically, specially to control oscillations, and overshoots in the vicinity of the steep gradients such as of shock waves, discontinuities, and

vortex sheets, where dissipation effects or shear stress take place in very thin layers of the flow, it is necessary to add numerical damping to the flow solver. An artificial viscosity model, as proposed by Argyris et al. (1990), is used due to its simplicity and efficiency in terms of CPU time. An artificial viscosity is added explicitly to the non-smoothed solution as follows

$$\mathbf{U}_s^{n+1} = \mathbf{U}^{n+1} + \mathbf{M}_L^{-1}\mathrm{D} \tag{16}$$

where $\mathbf{M}_L$ is the assembled lumped mass matrix, $\mathbf{U}_s^{n+1}$ and $\mathbf{U}^{n+1}$ are the smoothed and non-smoothed solutions at $t+\Delta t$, respectively. The vector D is given by

$$\mathrm{D} = \sum_{\mathrm{ele}} \mathrm{CFL}\ \mathrm{CAF}\ S_{ele} \left[\mathbf{M} - \mathbf{M}_L\right]_{ele} \mathbf{U}_{ele}^n \tag{17}$$

where *ele* is an index referred to a specific element, $\mathrm{CFL} = \Delta t / \Delta t_E$ is the local Courant-Friedrichs-Lewy number, CAF is an artificial damping coefficient given by the user, S_{ele} is a pressure sensor at element level obtained as an average of nodal values S_i. Values of S_i are components of the following assembled global vector

$$S_{\mathrm{i}} = \sum_{\mathrm{ele}} \frac{\left|\left(\mathbf{M} - \mathbf{M}_L\right)_{ele} \mathbf{p}\right|_i}{\left[\left|\mathbf{M} - \mathbf{M}_L\right|_{ele} \mathbf{p}\right]_i} \tag{18}$$

where **p** is the pressure vector of a specific element, the bars indicate that absolute values of the corresponding terms must be taken and, finally, **M** is the consistent mass matrix at element level.

The constant CAF must be specified with care in order to avoid interferences of artificial and physical viscosities. In this work $0.4 \le \mathrm{CAF} \le 0.7$ were adopted.

4 ADAPTIVE UNSTRUCTURED MESH REFINEMENT

The unstructured mesh-based CFD methodology has undergone considerable development in the last decade in term of both mesh generation and solution algorithm development. The concentration of the node in the mesh is very important to obtain good quality solutions. The nodes need to be concentrated in regions where some variable gradients are high with respect to a specific criterium.

Local physical phenomena in the flow are detected with error indicators or errors estimators. In this work, these error indicators take into account regions with low velocities, changes in velocity directions, velocity gradients, pressure gradients and internal energy gradients. The criterion for mesh adaptation is based in the normal distribution of the error indicators and their mean values and standard deviation. The adaptive process was performed using the *h*-refinement method. Details of the error indicators, mesh adaptation and the refinement process can be found in Popiolek and Awruch (2006).

This adaptive scheme has been validated with respect to analytical and experimental results for several regimes of incompressible and compressible flows (Popiolek and Awruch, 2006; Bono, Popiolek and Awruch, 2007; Bono, 2008).

5 NUMERICAL RESULTS

In this section one test case is presented in order to evaluate the accuracy, the capability and the performance of the two explicit Taylor-Galerkin schemes in the context of

structured/unstructured meshes applied to the solution of hypersonic flows. These programs do not take into account high temperature effects, such as, vibrational excitation and chemical reaction.

Although in the present work only two-dimensional (2-D) examples are presented, they were simulated with a three-dimensional solver taking one layer of elements in the *z*-direction, which is perpendicular to the flow direction. The boundary conditions are chosen so that a 2-D flow field is simulated. Fluid properties are considered constant, with $\gamma = 1.4$ and Prandtl Number Pr = 0.72.

5.1 Supersonic Flow past a Compression Corner (or "Wedge on a Flat Plate")

In this example the case 14 studied by Holden et al. (2006) is considered. This test case has been studied extensively using experimental and computational techniques. The fluid properties are given by a Mach number equal to 10.30 and a Reynolds number equal to 24624.6 (with relation to the values of the free stream conditions and the length of the flat plate, BC). With this example it is intended to validate the various schemes implemented and the method of adaptive refinement in hypersonic flow, as well as contribute to understanding the physical characteristics of the problem of shock wave / laminar boundary layer interaction.

The domain and boundary conditions for the problem of a flat plate with a ramp with 30 degrees of inclination are shown in Figure 2, being the dimensions AB = 0.5, BC = L = 4.004, BD = 8.661, AF = 0.5, DE = 5.0 and 0.01 in the perpendicular direction to the *xy* plane. The free stream conditions for the 14 case are: velocity $V_\infty = (10.30; 0.0; 0.0)$, specific mass $\rho_\infty = 1.0$, total energy $e_\infty = 54.83075$ and pressure $p_\infty = 0.71428$. The inflow boundary conditions were applied at the edges AF and FE. In AB are placed symmetry boundary conditions and the non slip boundary condition are imposed in BCG. Finally, in GE the boundary conditions are free. The values of the free stream conditions were taken as initial conditions and implemented in all the nodes in the domain except in the nodes with non slip boundary condition.

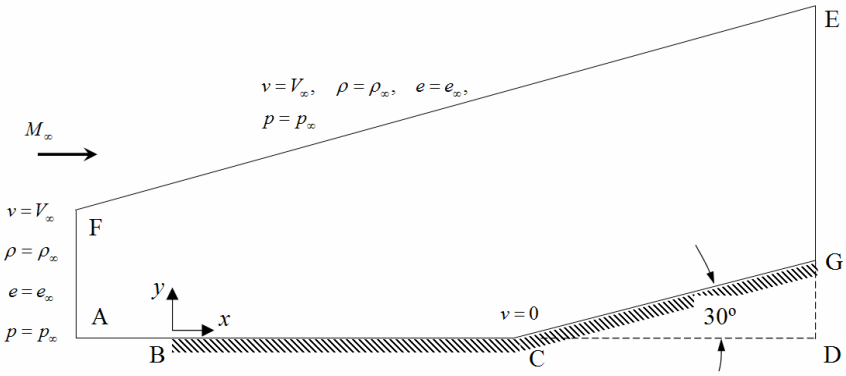

Figure 2: Computational domain and boundary conditions

The numerical schemes employed for the solution of the Navier-Stokes equations are the one-step and two-step schemes with hexahedral (H) and tetrahedral (T) elements. In order to capture de boundary layers effects the elements are concentrated near the solid contours (BCG). The mesh with tetrahedral elements is obtained by subdividing each hexahedral element into five tetrahedral elements. The identification for each example, the number of nodes (*nno*), the number of elements (*nele*), the number of nodes on the wall (*nnoCS*), the length (Δl) of the recirculation, the maximum pressure coefficient (CP_{max}), the minimum time

step (Δt) and the artificial damping coefficient (CAF) are shown in Table 1.

The meshes with tetrahedral elements are adapted with the following errors indicators: low velocity components, change in the velocity components, velocity gradients, pressure gradients and internal energy gradients. The first and second refinements are identified as R1 and R2, respectively. In Figure 3 are displayed details of the meshes used in the region of intersection of the flat plate with the ramp.

Mesh	*nno*	*nele*	*nnoCS*	Δl	Cp_{max}	Δt	CAF
M1H	31232	15300	482	0.551	0.967	4.10^{-5}	0.7
M2H	48422	23800	642	0.677	1.051	4.10^{-5}	0.7
M3H	68202	33600	782	0.706	1.058	3.10^{-5}	0.7
M3aH	68202	33600	782	0.743	1.123	3.10^{-5}	0.4
M2Hp2	48422	23800	642	0.741	1.055	4.10^{-5}	0.7
M2aHp2	48422	23800	642	0.764	1.128	4.10^{-5}	0.4
M2T	26112	63750	482	0.349	0.834	3.10^{-5}	0.7
M2TR1	66860	220131	1443	0.509	0.875	1.10^{-5}	0.7
M2TR2	246882	1067740	4805	0.542	0.998	6.10^{-6}	0.7
M2Tp2	26112	63750	482	0.269	0.786	3.10^{-5}	0.7
M2Tp2R1	66860	220131	1443	0.480	0.845	1.10^{-5}	0.7
M2Tp2R2	246882	1067740	4805	0.554	0.953	6.10^{-6}	0.7

Table 1: Numerical and physical parameters for the SWBLI simulation.

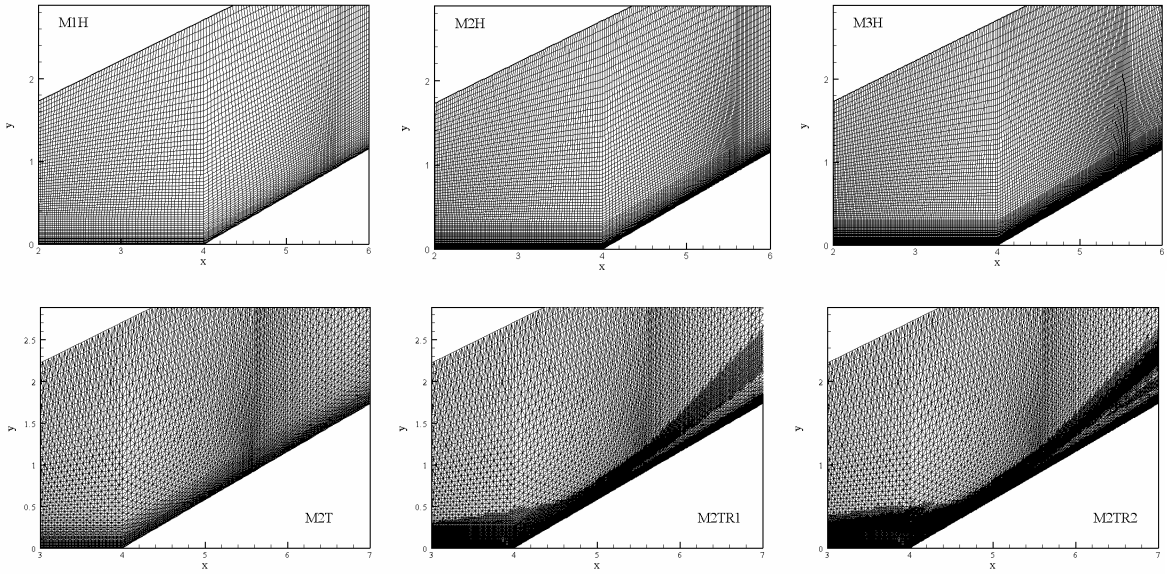

Figure 3: Details of the finite elements meshes around the flat-plate / ramp intersection

The Mach number contours for the mesh with hexahedral elements using the one-step iterative scheme (M1H, M2H and M3H) are shown in Figure 4. It is clear that the interaction

induces separation and a recirculation region is formed. We note that the main phenomena of the problem are perfectly captured by the mesh M3H, the recirculation zone increases with the successive refinements of the mesh.

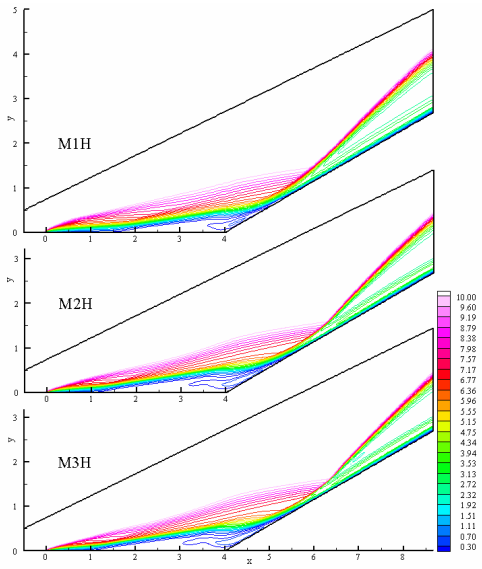

Figure 4: Mach number contours on the meshes M1H, M2H and M3H with hexahedral elements, using the one-step iterative scheme

The computed pressure coefficient and skin friction coefficient at the time t = 4.2 for the meshes M1H, M2H, M3H and M3aH are shown in Figure 5. In the last mesh the CAF was reduced from 0.70 to 0.40. The pressure coefficient is very close to the experimental results obtained by Holden et al. (2006) near the recompression region. However, in the recirculation region, in the peak pressure and in the plateau pressure, the numerical computation overestimate the pressure coefficient. The skin friction coefficient increases rapidly downstream of the attachment. The initial mesh M1H gives the best results compared with the experimental results in the recirculation region, but disagreement occurs with the successive refinements of the mesh. The meshes M2H and M3H show a recirculation region and peak pressures greater than those presented by Holden et al. (2006) and mesh M1H; these results are representative of a problem with an higher Reynolds number.

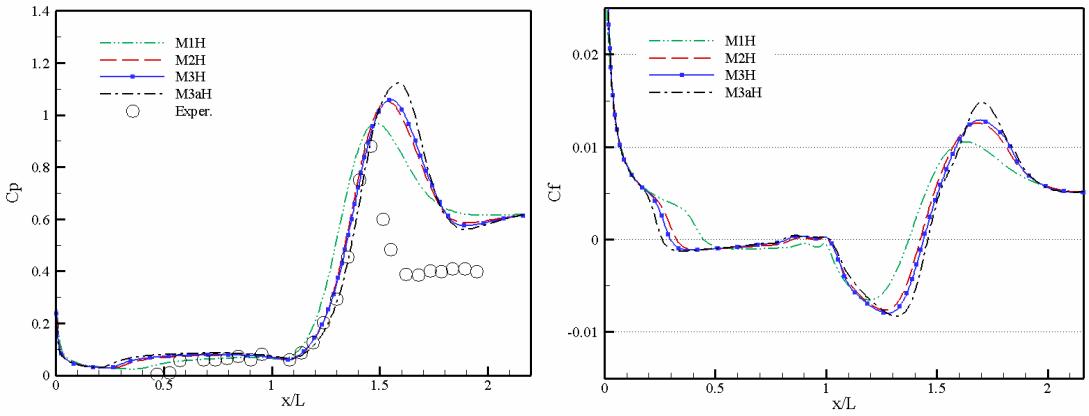

Figure 5: Pressure coefficient and skin friction coefficient on the meshes M1H, M2H, M3H and M3aH, compared with result obtained by Holden et al. (2006)

The differences between the experimental and numerical results can not be attributed to the mesh refinement, because the small difference between the pressure coefficient on the M2H and M3H meshes indicate that the solutions on those meshes may be regarded as nearly mesh independent.

The artificial damping coefficient was reduced from 0.7 to 0.4 in the mesh M3H with the aim of study its influence. Reduction of CAF (mesh M3aH) increases slightly the peak pressure and recirculation region compared with the previous results (see Figure 5).

The pressure coefficient and skin friction coefficient at the time t = 4.2 for the mesh with hexahedral elements using the two-step scheme (M2p2) are shown in Figure 6. The tests with the one-step and two-step schemes with hexahedral mesh look similar. For the same artificial damping coefficient (CAF = 0.7), the two-step scheme (M2Hp2) is more diffusive than the one-step scheme (M2H). Reducing the coefficient CAF to 0.4, no improvements are obtained in the results (see M2aHp2).

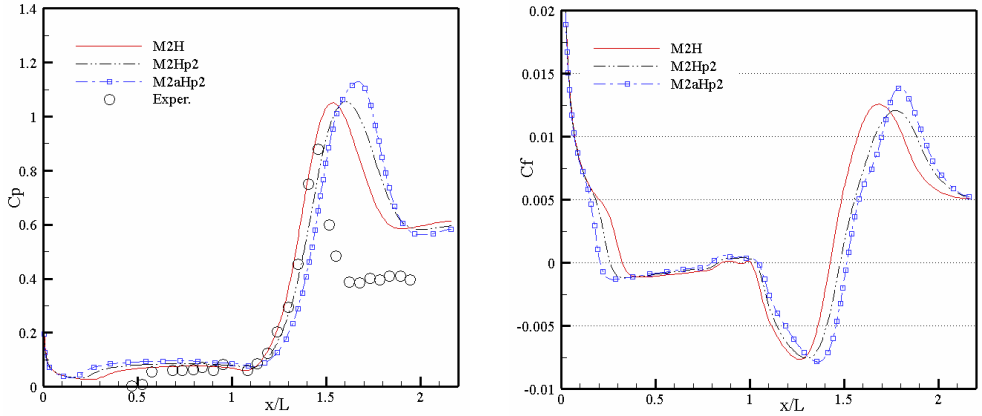

Figure 6: Pressure coefficient and skin friction coefficient on the mesh M2H using the one-step and two-step (p2) schemes

The discrepancies obtained with the hexahedral meshes, possibly have origin in the discretization used, since the refinement and the reduction of the CAF do not improve computational results. With an higher concentration of elements at the beginning of the plate and at the intersection flat-plate/ramp, probably the separation of the boundary layer would be best captured.

Contours of Mach number and specific mass for the meshes M2T, M2TR1 and M2TR2 with tetrahedral elements using the one-step scheme and the mesh adaption technique is shown in Figure 7. The recirculation and recompression regions and the reflected shock wave are efficiently resolved with a mesh refinement using an automatic adaptive technique.

The pressure coefficient and skin friction coefficient distributions, Cp and Cf, are shown in Figure 8. This plot demonstrates the important role of the adaptive mesh refinement in capturing physical phenomena. M2TR2 mesh (two refinements levels) shows a good agreement with the experimental results presented by Holden et al. (2006), mainly in the recirculation region and the position and value of peak pressure. The computational results determined with the hexahedral meshes in the recompression region (Figure 5) are slightly better than those obtained with tetrahedral meshes, but with the successive refinements the results in the M2T mesh are closer to those presented by Holden et al. (2006).

The value of the pressure coefficient in the plateau pressure region is approximately 0.61 with the M2T meshes; this value practically is coincident with the pressure coefficient obtained in the case of a non-viscous problem (Cp_{invisc} = 0.628). This difference is practically

the same to that obtained with the hexahedral meshes.

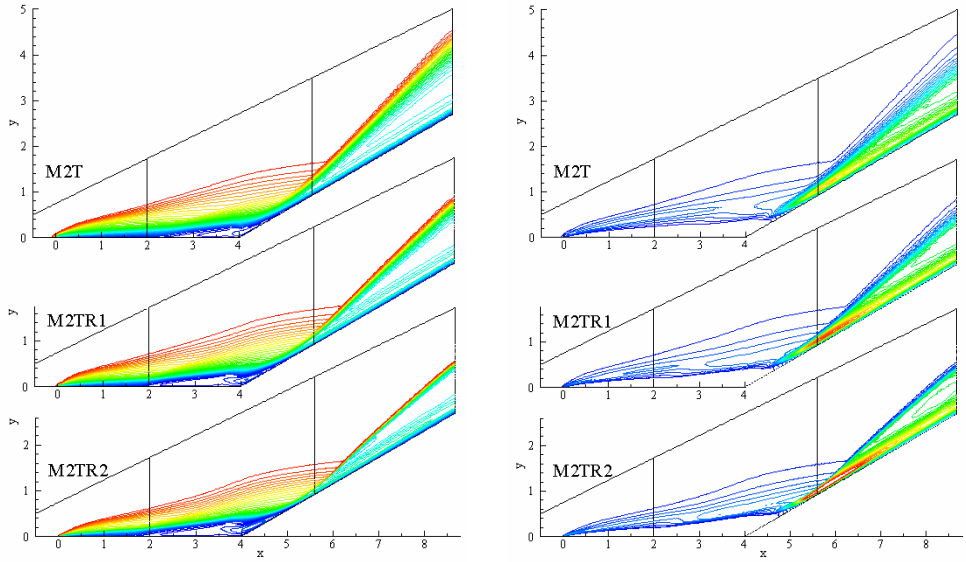

Figure 7: Mach number and specific mass contours on the meshes M2T, M2TR1 and M2TR2 with tetrahedral elements

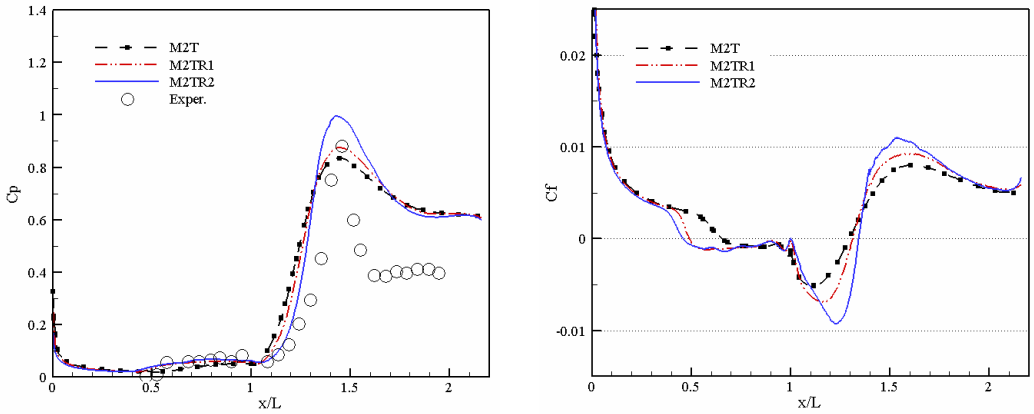

Figure 8: Pressure coefficient and skin friction coefficient on the meshes M2T, M2TR1 and M2TR2, compared with result obtained by Holden et al. (2006)

The pressure coefficient and skin friction coefficient at the time t = 4.428 using tetrahedral meshes M2TR2 (one-step scheme) and M2Tp2R2 (two-step scheme) are plotted on Figure 9, together with experimental and numerical results (Numer. 1 = Gnoffo , Numer. 2 = Tannehill) presented by Holden et al. (2006). Numerical results are in almost perfect agreement with the length of the interaction regions and the recompression region. The meshes M2T and M2Tp2 over predicted the pressures in the forebody region.

As shown in Figure 9, while Gnoffo and Tannehill predictions of the pressure peak achieve excellent agreement with experiments, the present computational results (M2TR2 and M2Tp2R2) overpredicts the pressure peak region. Nevertheless, the position of the peak pressure is better captured with the present simulation.

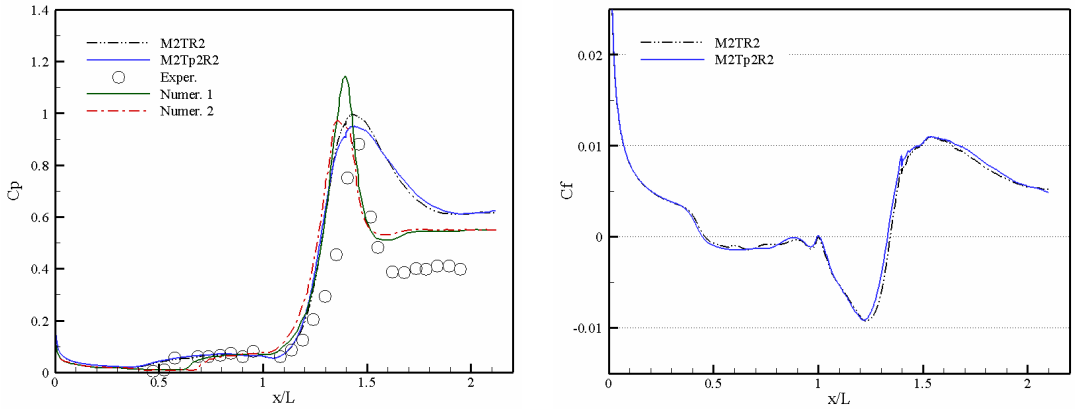

Figure 9: Pressure coefficient and skin friction coefficient on the meshes M2TR2 (one-step scheme) and M2Tp2R2 (two-step scheme), compared with result obtained by Holden et al. (2006)

Finally, with the purpose of analyzing the mechanism of shock wave / laminar boundary layer interaction, the pressure coefficient and skin friction coefficient in Figure 10 shows the formation of a recirculation region and a shock wave at different non-dimensional times in the meshes M2T, M2TR1 and M2TR2. During the first stage (t = 0.21) is formed a small recirculation region (negative Cf) in the intersection region between the flat-plate and the ramp ($x / L = 1.0$). After this point the pressure has a slight peak due to the compression wave reattachment. After the recompression region the pressure value is approximately, Cp = 0.60, while for non-viscous problem Cp is about 0.628.

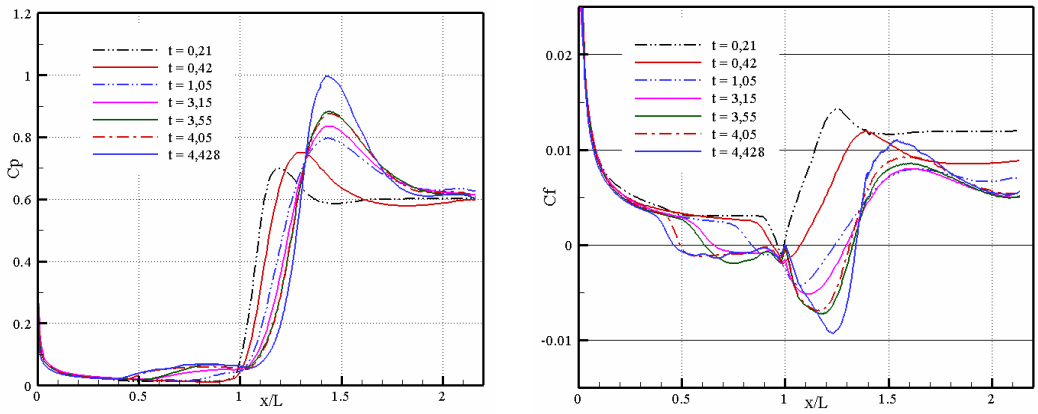

Figure 10: Pressure coefficient and skin friction coefficient on the meshes M2T/R1/R2 at different non-dimensional times

It should be noted that with time increase, the separation region length also increases. Initially the growth is greater on the flat-plate, and later on the ramp. The point of boundary layer reattachment remains practically fixed when time reaches $t = 3.15$, but the point of boundary layer separation moves continuously until $t = 4.428$. It must be observed that for the last two times showed in Figure 10 ($t = 4.05$ and 4.428) the recirculation region grows less in comparison with the growth of the pressure peak.

The computed velocities profiles (v_1 and v_2) at stations $x / L = 0.25$, 0.5, 0.75, 1.0, 1.25, 1.40, 1.50 and 1.75 at the time t = 4.428 are displayed in Figure 11. The abscissa is the component of velocity, and the ordinate is the distance measured normal to the wall. In Holden et al. (2006), the authors did not report experimental data for velocities, pressure and specific mass profiles.

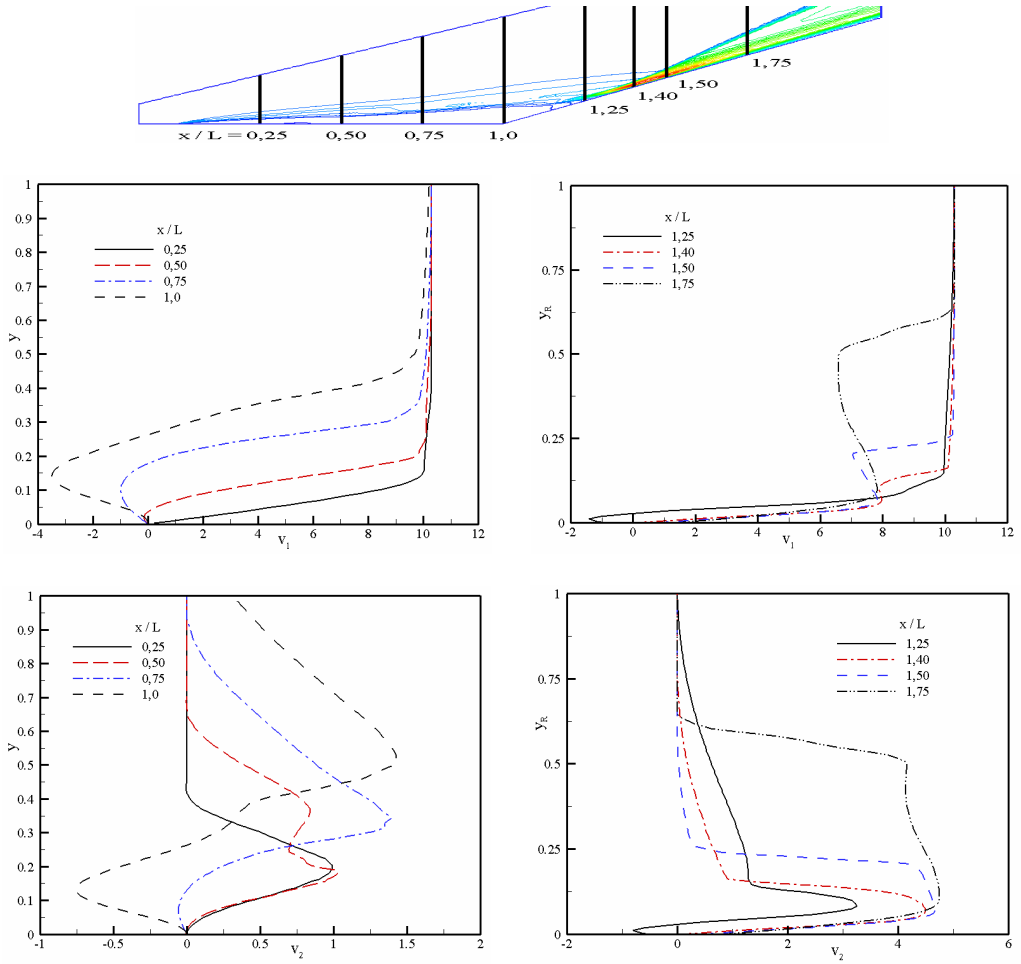

Figure 11: Velocities profiles (v_1 and v_2) at different stations (x/L)

The profile $x / L = 0.25$, is located upstream of the separation line and $x / L = 1.25$ is located downstream of the reattachment point. The skin friction coefficient increases rapidly downstream of the attachment due to the increase of the gradient on the stations $x / L = 1.40$ and 1.50. The distortion of velocity profile is due to the shocks generated by the leading edge and the recirculation region.

Specific mass and pressure profiles are shown in Figures 12 and 13. It can be observed that the specific mass and the pressure increase considerably after the reattachment point ($x / L =$ 1.40 and 1.50).

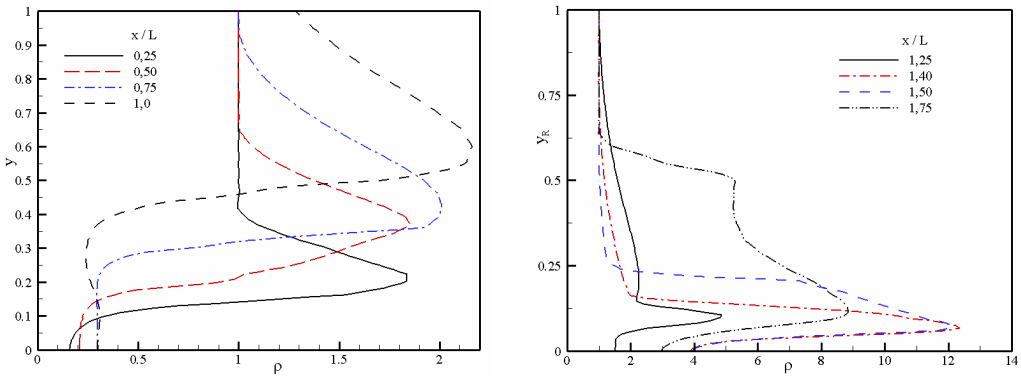

Figure 12: Specific mass profiles at different stations (x/L)

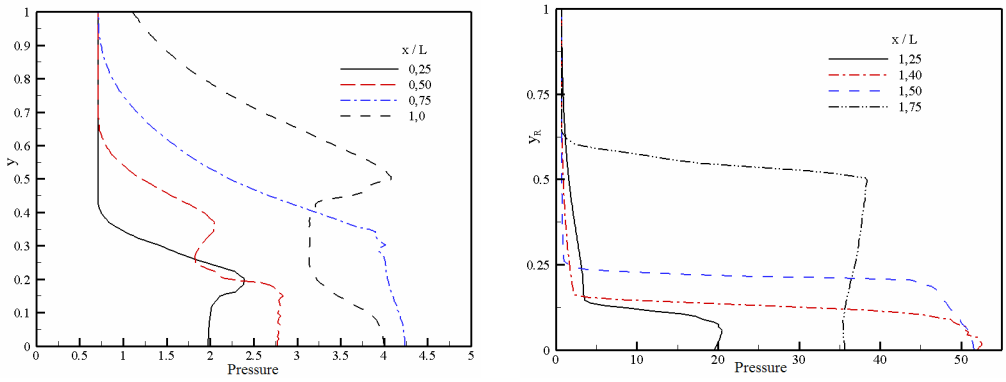

Figure 13: Pressure profiles at different stations (*x/L*)

6 CONCLUSIONS

The computations of the shock wave/laminar boundary layer interaction over a compression corner have been performed by two explicit Taylor-Galerkin schemes in the context of meshes with hexahedral and tetrahedral elements. Based on the simulations examined in this study, no clear advantage was observed in choosing one scheme over the other.

The results presented in this paper have shown that the tetrahedral mesh with an adaptive technique presented solutions with better quality than the solution using hexahedral meshes.

In the best Navier-Stokes solution the structure of the flow field was captured quite exactly with respect to the experimental model. The detailed characteristics of the distributions of pressure through the interaction regions were well predicted. A slight disagreement of the pressure on the forebody region was obtained. More tests need to be done to understand why the numerical solutions with hexahedral elements are inaccurate in some regions.

Based on the results obtained here, it may be concluded that an automatic adaptive technique have produced important improvements. Error indicators for low velocity components, change in the velocity direction, velocity gradients, pressure gradients and internal energy gradients, together with a mesh adaptation criterion identify correctly regions where refinements were necessary to obtain more accurate solutions. This test case also show that the use of a mesh adaptation procedure relieves the user from the tedious task of constructing an appropriate mesh and leads to a really optimal mesh that substantially reduces the amount of artificial dissipation needed in the flow solver.

ACKNOWLEDGEMENTS

The authors gratefully acknowledge the support of the CAPES and CNPq.

REFERENCES

J. Argyris, I.S. Doltsinis and H. Friz. Study on computational reentry aerodynamics. *Computer Methods in Applied Mechanics and Engineering*, 81:257–289, 1990.

J.J. Bertin. *Hypersonic Aerothermodynamics*, AIAA Education Series, USA , 1994.

G. Bono, T.L. Popiolek and A.M. Awruch. Estrategia de Adaptación de Mallas para Problemas Aeroespaciales y Aeronáuticos, *Mecánica Computacional*, 26, 3117-3133, 2007.

G. Bono. Simulação *Numérica de Escoamentos em Diferentes Regimes utilizando o Método*

dos Elementos Finitos (text in portuguese), Doctoral Thesis, PROMEC, UFRGS, Brazil, 2008.

B. Chanetz, R. Benay, J.M. Bousquest, R. Bur, T. Pot, F. Grasso, J. Moss. Experimental and Numerical Study of the Laminar Separation in Hypersonic Flow, *Aerosp. Scien. and Technology*, 3, 205-218, 1998

J. Delery. Shock/shock and shock-wave/boundary layer Interactions in Hypersonic Flows, *AGARD-R-761*, 1988.

D.S. Dolling. Fifty Years of Shock-Wave/Boundary-Layer Interaction Research: What Next ?, *AIAA Journal*, 39 (8), 1517-1531 , 2001.

J. Donea. A Taylor-Galerkin for convective transport problems. *International Journal for Numerical Methods in Engineering*, 20:101–119, 1984.

M.S. Holden, T.P. Waldhams, J.K Harvey and G.V. Candler. Comparison between Measurements in Regions of Laminar Shock Wave Boundary Layer Interaction in Hypersonic Flows with Navier-Stokes and DSMC Solutions, *OTAN RTO-TR-AVT-007-V3*, 2006.

T.J.R. Hughes and T.E. Tezduyar. Finite element methods for first-order hyperbolic systems with particular emphasis on the compressible Euler equations. *Computer Methods in Applied Mechanics and Engineering*, 45:217–284, 1984.

F. Grasso and M. Marini. Analysis of Hypersonic Shock-wave Laminar Boundary-layer Interaction Phenomena, *Computer & Fluids*, 25, 561-581, 1996.

M. Kawahara and H. Hirano. A finite element method for high Reynolds number viscous fluid flow using two step explicit scheme. *International Journal for Numerical Methods in Fluids*, 3:137–163, 1983.

F.W. White. *Viscous fluid flow*. McGraw Hill, USA, 1974.